Geoscientific
Model Development
Discussions

(GO)²-SIM: A GCM-Oriented Ground-Observation Forward-Simulator Framework for Objective Evaluation of Cloud and Precipitation Phase

Katia Lamer[1], Ann M. Fridlind.[2], Andrew S. Ackerman.[2], Pavlos Kollias[3,4,5],
Eugene E. Clothiaux[1] and Maxwell Kelley[2]

[1] Department of Meteorology and Atmospheric Science, Pennsylvania State University, University Park, 16802, U.S.A.
[2] NASA Goddard Institute for Space Studies, New York, 10025, U.S.A.
[3] Environmental & Climate Sciences Department, Brookhaven National Laboratory, Upton, 11973, U.S.A.
[4] School of Marine and Atmospheric Sciences, Stony Brook University, Stony Brook, 11794, U.S.A.
[5] University of Cologne, Cologne, 50937, Germany

Correspondence to: Katia Lamer (kxl5431@psu.edu)

Abstract

General circulation model (GCM) evaluation using ground-based observations is complicated by inconsistencies in hydrometeor and phase definitions. Here we describe (GO)²-SIM, a forward-simulator designed for objective hydrometeor phase evaluation, and assess its performance over the North Slope of Alaska using a one-year GCM simulation. For uncertainty quantification, 18 empirical relationships are used to convert model grid-average hydrometeor (liquid and ice, cloud and precipitation) water contents to zenith polarimetric micropulse lidar and Ka-band Doppler radar measurements producing an ensemble of 576 forward-simulation realizations. Sensor limitations are represented in forward space to objectively remove from consideration model grid cells with undetectable hydrometeor mixing ratios, some of which may correspond to numerical noise.

Phase classification in forward space is complicated by the inability of sensors to measure ice and liquid signals distinctly. However, signatures exist in lidar-radar space such that thresholds on observables can be objectively estimated and related to hydrometeor phase. The proposed phase classification technique leads to misclassification in fewer than 8% of hydrometeor-containing grid cells. Such misclassifications arise because, while the radar is capable of detecting mixed-phase conditions, it can mistake water- for ice-dominated layers. However, applying the same classification algorithm to forward-simulated and observed fields should generate hydrometeor phase statistics with similar uncertainty. Alternatively, choosing to disregard how sensors define hydrometeor phase leads to frequency of occurrence discrepancies of up to 40%. So, while hydrometeor phase maps determined in forward space are very different from model "reality" they capture the information sensors can provide and thereby enable objective model evaluation.

Geoscientific
Model Development
Discussions

1 Introduction

The effect of supercooled water on the Earth's top-of-atmosphere energy budget is a subject of increasing interest owing to its wide variability across climate models and its potential impact on predicted equilibrium climate sensitivity (Tan et al., 2016; McCoy et al., 2016; Frey et al., 2017). Some general circulation models (GCMs) now prognose number concentrations and mass mixing ratios for both cloud and precipitation hydrometeors of both liquid and ice phase, which enables them to shift towards more realistic microphysical process-based phase prediction (e.g., Gettelman and Morrison, 2015; Gettelman et al., 2015). While more complete and physically sound, these models still contain multiple scheme choices and tuning parameters, creating a need for increasingly thorough evaluation and adjustment (e.g., Tan and Storelvmo, 2016; English et al., 2014).
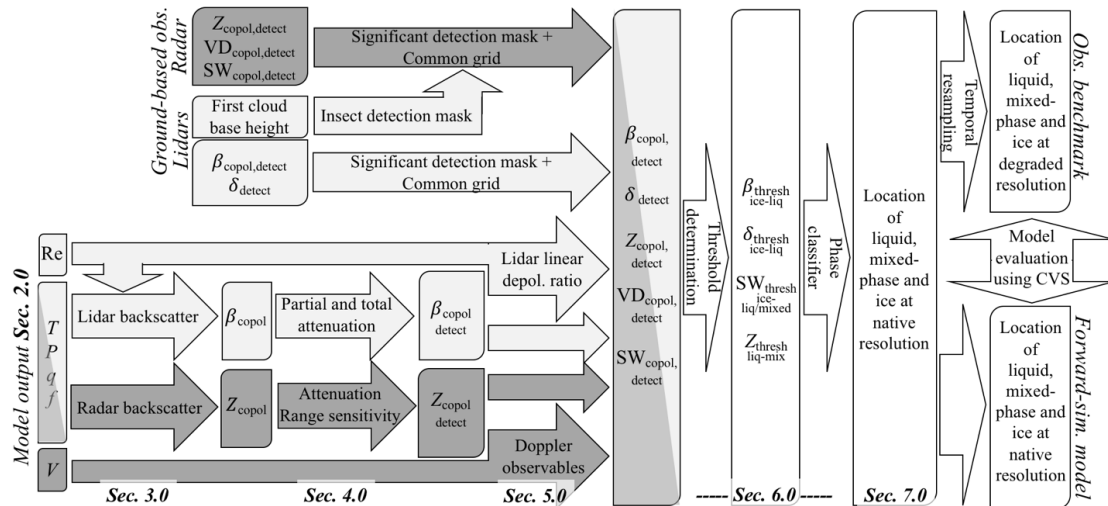
Active remote sensing observations remain an indirect approach to evaluate models because they measure hydrometeor properties different from those produced by microphysical schemes. For each hydrometeor species within a grid cell models prognose geophysical quantities such as mass and number concentration, whereas active remote sensors measure power backscattered from all hydrometeors species present within their observation volumes. Defining which hydrometeors have an impact is a fundamental question that needs to be addressed by the modeling, as well as observational, communities. In numerical models it is not uncommon to find very small hydrometeor mixing ratio amounts as demonstrated below. They may possibly be unphysical, effectively numerical noise, and the decision of which hydrometeor amounts are physically meaningful is somewhat arbitrary. Considering sensor capabilities is one path to objectively assessing hydrometeor populations within models. On such a path it is possible to evaluate those simulated hydrometeor populations that lead to signals detectable by sensors, leaving unassessed those not detected. Sensor detection capabilities are both platform- and sensor-specific. Space-borne lidars can adequately detect liquid clouds globally but their signals cannot penetrate thick liquid layers, limiting their use to a subset of single-layer systems or upper-level cloud decks (Hogan et al., 2004). Space-borne radar observations, while able to penetrate multi-layer cloud systems, are of coarser vertical resolution and of limited value near the surface owing to ground interference and low sensitivity (e.g., Huang et al., 2012b; Battaglia and Delanoë, 2013; Huang et al., 2012a). A perspective from the surface can therefore be more appropriate for the study of low-level cloud systems (e.g., de Boer et al., 2009; Dong and Mace, 2003; Klein et al., 2009; Intrieri et al., 2002).

Fortunately, both sensor sampling and hydrometeor scattering properties can be emulated through the use of forward-simulators. Forward-simulators convert model output to quantities observed by sensors and enable a fairer comparison between model output and observations; discrepancies can then be more readily attributed to dynamical and microphysical differences rather than methodological bias. For example, the CFMIP (Cloud Feedback Model Intercomparison Project) Observation Simulator Package (COSP) is composed of a number of satellite-oriented forward-simulators (Bodas-Salcedo et al., 2011), including a lidar backscattering forward-simulator that has been used to evaluate the representation of upper-level supercooled water layers in GCMs (e.g., Chepfer et al., 2008; Kay et al., 2016). Also, Zhang et al. (2017) present a first attempt at a ground-based radar reflectivity simulator tailored for GCM evaluation.

Here we propose to exploit the complementarity of ground-based vertically pointing polarimetric lidar and Doppler radar measurements, which have been shown uniquely capable of documenting water phase in shallow and multi-layered cloud conditions near the surface where supercooled water layers frequently form. More specifically, we present a GCM-oriented ground-based observation forward-simulator [(GO)^2-SIM] framework designed for objective hydrometeor phase evaluation (Fig. 1). GCM output variables (Sec. 2) are converted to observables in three steps: 1) hydrometeor backscattered power estimation (Sec. 3), 2) consideration for sensor capabilities (Sec. 4) and, 3) estimation of specialized observables (Sec. 5). These

Geoscientific
Model Development
Discussions

Figure 1. (GO)²-SIM framework. (GO)²-SIM treats/emulates two types of remote sensors: Ka-band Doppler radars (dark gray shading) and 532 nm polarimetric lidars (light gray shading). It then tunes and applies a common phase-classification algorithm (white boxes) to both observed (upper section) and forward-simulated (bottom section) fields. Follow-on work will show how an approach based on cloud vertical structure (CVS) can be used as a final step before model evaluation.

forward-simulated fields, similar to observed fields, are used as inputs to a multi-sensor water phase classifier (Sec. 6). The performance of (GO)²-SIM is evaluated over the North Slope of Alaska using output from a one-year simulation of the current development version of the NASA Goddard Institute for Space Studies GCM, hereafter referred to by its generic name, ModelE. Limitations are discussed in Sec. 6.3 and uncertainty quantified in Sec. 7.
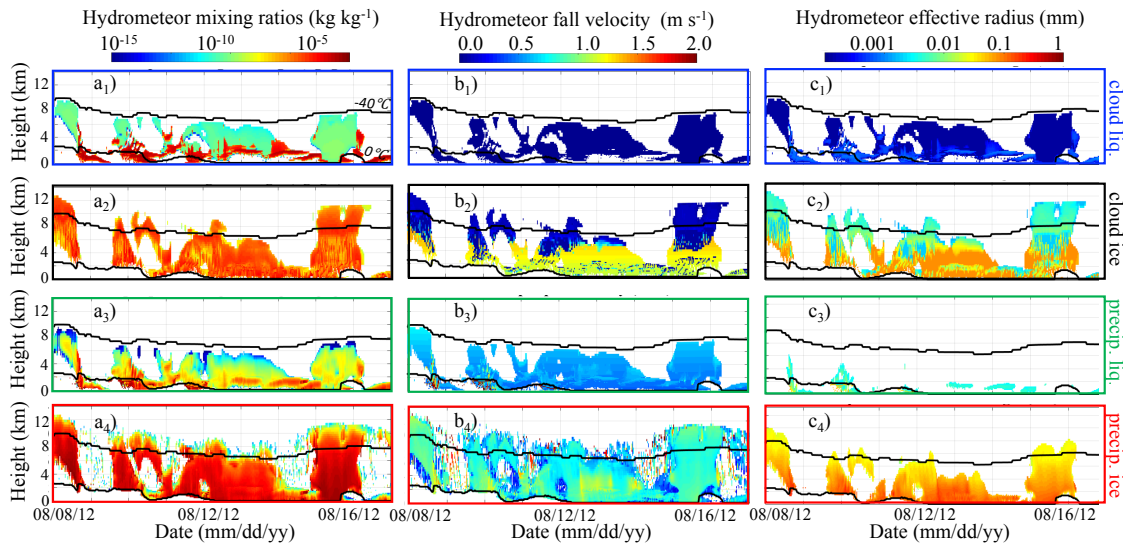
2 GCM Outputs Required as Inputs to the Forward-Simulator

To demonstrate how atmospheric model variables are converted to observables we performed a one-year global simulation using the current development version of the ModelE GCM. Outputs from a column over the North Slope of Alaska (column centered at latitude 71.00° and longitude -156.25°) are input to (GO)²-SIM. The most relevant changes from a recent version of ModelE (Schmidt et al. 2014) are implementation of the Bretherton and Park (2009) moist turbulence scheme and the Gettelman and Morrison (2015) microphysics scheme for stratiform cloud. The implementation of a two-moment microphysics scheme with prognostic precipitation species makes this ModelE version more suitable for the forward simulations presented here than previous versions. Here ModelE is configured with a 2.0° by 2.5° latitude-longitude grid with 62 vertical layers. The vertical grid varies with height from 10 hPa layer thickness over the bottom 100 hPa of the atmosphere, coarsening to about 50 hPa thickness in the mid-troposphere, and refining again to about 10 hPa thickness near the tropopause. For the current study, model top is at 0.1 hPa, though we limit our analysis to pressures greater than 150 hPa. Dynamics (large scale advection) is computed on a 225-s time step and column physics on a 30-min time step. High time-resolution outputs (every column physics time step) are used as input to (GO)²-SIM. ModelE relies on two separate schemes to prognose the occurrence of stratiform and convective clouds. The current study focuses on stratiform clouds because their properties are more thoroughly diagnosed in this model version; when performing future model evaluation, the contribution from convective clouds will also be considered.

Geoscientific
Model Development
Discussions

Figure 2. Sample time series of ModelE outputs: a_{1-4}) mixing ratios, b_{2-4}) mass weighted fall speed (positive values indicate downward motion) and c_{1-4}) effective radii for cloud droplets (1; blue boxes), cloud ice particles (2; black boxes), precipitating liquid drops (3; green boxes) and precipitating ice particles (4; red boxes). Also indicated are the locations of the 0 °C and -40 °C isotherms (horizontal black lines).

An example of eight days of this simulation is displayed in Fig. 2. From a purely numerical modelling standpoint, the simplest approach to defining hydrometeors is to consider any nonzero hydrometeor mixing ratio as physically meaningful. Using this approach, we find that 43.5 % of the 981,120 grid cells simulated in the one-year ModelE run contain hydrometeors, with 2.4 % of them being pure liquid, 37.8 % pure ice and 59.8 % mixed in phase (Table 1a). However, these statistics are impacted by a number of simulated small hydrometeor mixing ratio amounts that may or may not result from numerical noise (e.g., Fig. 2a; blue-green colors). The forward-simulator framework will be used to create phase statistics of only those hydrometeors present in amounts that can create signal detectable by sensors hence removing the need for arbitrary filtering.

$(GO)^2$-SIM forward-simulator inputs are, at model native resolution, mean grid box temperature and pressure as well as hydrometeor mixing ratios, area fractions (used to estimate in-cloud values), mass weighted fall speeds and effective radii for four hydrometeor species: cloud liquid water, cloud ice, precipitating liquid water and precipitating ice. In its current setup, $(GO)^2$-SIM can accommodate any model that produces these output variables

3 Hydrometeor Backscattered Power Simulator

Reaching a common objective hydrometeor definition between numerical model output and active sensors starts by addressing the fact that they are based on different hydrometeor properties (i.e., moments). Backscattering amounts, observed by sensors, depend on both sensor frequency and on hydrometeors properties and amounts. Hydrometeor properties that impact backscattering include hydrometeor size, phase, geometrical shape, orientation and bulk density. In most GCMs, however, such detailed information is highly simplified (e.g., spherical ice particles) or not explicitly represented (e.g., orientation), which introduces uncertainty in the process of transforming model output to observables.

Geoscientific
Model Development
Discussions

165 **Table 1.** a) Hydrometeor phase frequency of occurrence obtained a) from ModelE mixing ratios outside of
166 the forward-simulator framework, b) and c) from the forward simulation ensemble created using different
167 backscattered power assumptions. The median and interquartile range (IQR) capture the statistical behavior
168 of the ensemble. Results using thresholds b) objectively determined for each forward ensemble member, c)
169 modified from those in Shupe (2007). Percentage values are relative either to the total number of simulated
170 hydrometeor-containing grid cells (426,603) or those grid cells with detectable hydrometeor amounts
171 (333,927). Note that the total number of simulated grid cells analyzed is 981,120.

172

a) Determined using ModelE Output Hydrometeor Mixing Ratios			
	Grid cells containing only liquid phase	Grid cells containing mixed phase	Grid cells containing only ice phase	Simulated hydrometer-containing grid cells
Frequency of Occurrence (%)	2.4	59.8	37.8	43.5

b) Determined Using Flexible Objective Thresholds from Model Output Mixing-Ratios								
	Grid cells classified as liquid phase		Grid cells classified as mixed phase		Grid cells classified as ice phase		Grid cells containing detectable hydrometeors	
	Median	½ IQR	Median	½ IQR	Median	½ IQR	Median	½ IQR
Frequency of Occurrence (%)	11.3 ±	0.6	19.2 ±	1.8	68.8 ±	3.1	78.3 ±	1.8
False Positive (%)	0.5 ±	0.0	1.1 ±	0.3	0.0 ±	0.0	1.7 ±	0.3
False Negative (%)	0.2 ±	0.0	See questionable row		1.5 ±	0.2	1.7 ±	0.3
Questionable (%)	1.4 ±	0.0			3.8 ±	0.9	5.2 ±	0.9
Total Error (%)							6.9 ±	1.1

c) Determined Using Fixed Thresholds Modified from Shupe (2007)								
	Grid cells classified as liquid phase		Grid cells classified as mixed phase		Grid cells classified as ice phase		Grid cells containing detectable hydrometeors	
	Median	½ IQR	Median	½ IQR	Median	½ IQR	Median	½ IQR
Frequency of Occurrence (%)	12.5 ±	0.4	13.1 ±	2.4	71.5 ±	3.7	78.2 ±	1.8
False Positive (%)	0.5 ±	0.0	0.3 ±	0.0	0.1 ±	0.0	0.9 ±	0.0
False Negative (%)	0.1 ±	0.0	See questionable row		0.7 ±	0.0	0.9 ±	0.0
Questionable (%)	1.4 ±	0.0			5.3 ±	1.1	6.7 ±	1.1
Total Error (%)							7.6 ±	1.1

173
174

3.1 Lidar Backscattered Power Simulator

175
176
177   At a lidar wavelength of 532 nm, backscattered power is proportional to total particle cross section per
178 unit volume. Owing to their high number concentrations, despite their small size, cloud particles
179 backscatter this type of radiation the most.
180
181   In the Cesana and Chepfer (2013) backscattering-simulator, Mie theory is used to convert hydrometeor
182 effective radius to backscattered power; in such an approach cloud particles (both liquid and ice) are
183 assumed spherical. To avoid having to rely on this assumption for ice particles, (GO)^2-SIM employs
184 empirical relationships. We adopt the Hu et al. (2007b) representation of liquid cloud extinction derived
185 from CALIPSO and CERES-MODIS observations and retrievals of liquid water content and effective

186 radius (Table 2, Eq. 1). For cloud ice water content, a number of empirical relationships with lidar
187 extinction have been proposed for various geophysical locations and ice cloud types using a variety of
188 assumptions. Four of these empirical relationships are implemented in (GO)²-SIM (Table 2, Eqns. 2-5 and
189 references therein). These relationships will be used to create an ensemble of forward simulations that will
190 be used for uncertainty quantification (see Sec. 7). Using these empirical relationships, a given water
191 content can be mapped to a range of lidar extinction values (Fig. 3a). This spread depends both on the
192 choice of empirical relationships and on the variability of the atmospheric conditions that affect them (i.e.,
193 atmospheric temperature and hydrometeor effective radius variability). Fig. 3a also illustrates the
194 fundamental idea that lidar extinction increases with increasing water content and that for a given water
195 content cloud droplets generally lead to higher lidar extinction than cloud ice particles.

196

197 Lidar co-polar backscattered power ($\beta_{copol,species}$ [m^{-1}sr^{-1}]) generated by each hydrometeor species is
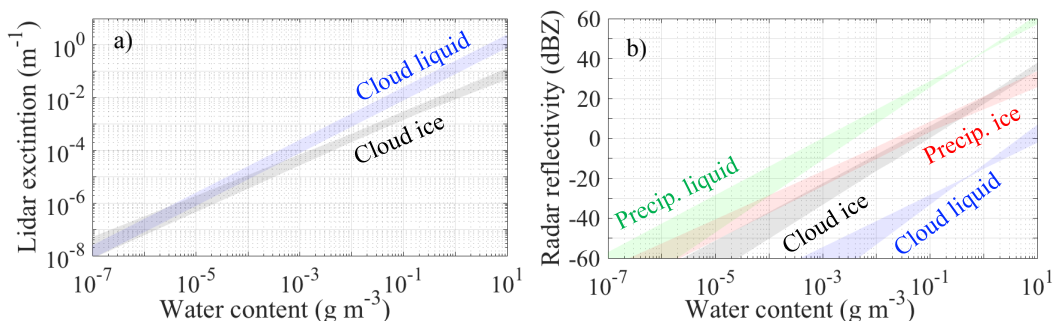198 related to lidar extinction ($\sigma_{copol,species}$ [m^{-1}]) through the lidar ratio:

199

200 $\beta_{copol,cl} = (1/18.6\ sr)\ \sigma_{copol,cl}.$ (O'Connor et al., 2004) (6)
201 $\beta_{copol,ci} = (1/25.7\ sr)\ \sigma_{copol,ci}.$ (Kuehn et al., 2016) (7)

202

203 Of course, lidars do not measure cloud droplet backscattering independently of cloud ice particle
204 backscattering. Rather they measure total co-polar backscattered power ($\beta_{copol,total}$) which the sum of the
205 contribution from both cloud phases.

206

3.2 Radar Backscattered Power Simulator

208

209   At the cloud-radar wavelength of 8.56 mm (Ka-band), backscattered power is approximately related to
210 the sixth power of the particle diameter, and inversely proportional to the forth power of the wavelength.
211 Hereafter radar backscattered power will be referred to as "radar reflectivity" as commonly done in
212 literature.

213

214 For reference, the COSP (Bodas-Salcedo et al., 2011) and ARM Cloud Radar Simulator for GCM (Zhang
215 et al., 2017) packages both use QuickBeam for the estimation of radar reflectivity (Haynes et al., 2007).
216 QuickBeam computes radar reflectivity using Mie theory and assuming all hydrometeor species to be
217 spherical and of a specified density.

218

219

221 **Figure 3.** a) Lidar extinction as a function of water content in the form of water cloud (blue) and ice cloud
222 (black). b) Radar co-polar reflectivity as a function of water content in the form of water cloud (blue) and
223 precipitation (green) and ice cloud (black) and precipitation (red). Spread emerges from using multiple
224 differing empirical relationships (listed in Table 2) and from variability in the one-year ModelE output
225 (including the effects of varying temperature and effective radii).

Geoscientific
Model Development
Discussions

Table 2. Empirical relationships used to convert hydrometeor water content (WC [g m^{-2}]) to lidar extinction (σ [m^{-1}]) and radar reflectivity (Z [mm^6 m^{-3}]).

Type	Eq. #	Relationships for lidar extinction	References
Cloud liq. (cl)	1	$\sigma_{copol,cl} = \dfrac{WC_{cl}(3/2)}{Re\ \rho_{liq}}$ with $\rho_{liq} = 1$	Hu et al. (2007b)
Cloud ice (ci)	2	$\sigma_{copol,ci} = \left(\dfrac{WC_{ci}}{119}\right)^{1/1.22}$	Heymsfield et al. (2005)
	3	$\sigma_{copol,ci} = \left(\dfrac{WC_{ci}}{a_3}\right)^{1/b_3}$ with $a_3 = 89 + 0.6204T$ and $b_3 = 1.02 - 0.0281T$	Heymsfield et al. (2005)
	4	$\sigma_{copol,ci} = \left(\dfrac{WC_{ci}}{527}\right)^{1/1.32}$	Heymsfield et al. (2014)
	5	$\sigma_{copol,ci} = \left(\dfrac{WC_{ci}}{a_2}\right)^{1/b_2}$ with $a_2 = 0.00532 * (T + 90)^{2.55}$ and $b_2 = 1.31e^{(0.0047T)}$	Heymsfield et al. (2014)

Type	Eq. #	Relationships for radar reflectivity	References
Cloud liq. (cl)	8	$Z_{copol,cl} = 0.048\ WC_{cl}^{2.00}$	Atlas (1954)
	9	$Z_{copol,cl} = 0.03\ WC_{cl}^{1.31}$	Sauvageot and Omar (1987)
	10	$Z_{copol,cl} = 0.031\ WC_{cl}^{1.56}$	Fox and Illingworth (1997)
Cloud ice (ci)	11a	$Z_{copol,ci} = 10^{\left(\frac{\log_{10}(WC_{ci})+1.70+0.0233\,T}{0.072}/10\right)}$	R. J. Hogan et al. (2006)
	12	$Z_{copol,ci} = \left(\dfrac{WC_{ci}}{0.064}\right)^{\frac{1}{0.58}}$	Atlas et al. (1995)
	13	$Z_{copol,ci} = \left(\dfrac{WC_{ci}}{0.097}\right)^{\frac{1}{0.59}}$	Liu and Illingworth (2000)
	14	$Z_{copol,ci} = \left(\dfrac{WC_{ci}}{0.037}\right)^{\frac{1}{0.696}}$	Sassen (1987)
Precip. liq (pl)	15	$Z_{copol,pl}[\text{mm}^6\,\text{m}^{-3}] = \left(\dfrac{WC_{pl}}{0.0034}\right)^{\frac{7}{4}}$	Hagen and Yuter (2003)
	16	$Z_{copol,pl}[\text{mm}^6\,\text{m}^{-3}] = \left(\dfrac{WC_{pl}}{0.0039}\right)^{\frac{1}{0.55}}$	Battan (1973)
	17	$Z_{copol,pl} = \left(\dfrac{WC_{pl}}{0.00098}\right)^{\frac{1}{0.7}}$	Sekhon and Srivastava (1971)
Precip. ice (pi)	11b	$Z_{copol,pi} = 10^{\left(\frac{\log_{10}(WC_{pi})+1.70+0.0233\,T}{0.072}/10\right)}$	R. J. Hogan et al. (2006)
	18	$Z_{copol,pi} = \left(\dfrac{WC_{pi}}{0.0218}\right)^{\frac{1}{0.79}}$	Liao and Sassen (1994)
	19	$Z_{copol,pi} = \left(\dfrac{WC_{pi}}{0.04915}\right)^{\frac{1}{0.90}}$	Sato et al. (1981)
	20	$Z_{copol,pi} = \left(\dfrac{WC_{pi}}{0.05751}\right)^{\frac{1}{0.736}}$	Kikuchi et al. (1982)

Geoscientific
Model Development
Discussions

229 In contrast, (GO)^2-SIM relies on water content-based empirical relationships to estimate cloud liquid water
230 (cl), cloud ice (ci), precipitating liquid water (pl) and precipitating ice (pi) radar reflectivity. It is expected
231 that these empirical relationships capture at least part of the impacts of hydrometeor non-sphericity and
232 inhomogeneity. A number of empirical relationships link hydrometeor water content to co-polar radar
233 reflectivity. Thirteen of these empirical relationships are implemented in (GO)^2-SIM (Table 2, Eqns. 8-20
234 and references therein). These relationships are used to create an ensemble of forward simulations for
235 uncertainty quantification (see Sec. 7). Figure 3b illustrates the fact that for all these empirical relationships
236 increasing water content leads to increasing radar reflectivity. As already mentioned, radar reflectivity is
237 approximately related to the sixth power of the particle diameter, which explains why, for the same water
238 content, precipitating hydrometeors are associated with greater reflectivity than cloud hydrometeors.
239
240 In reality, radars cannot isolate energy backscattered by individual hydrometeor species. Rather they
241 measure total co-polar reflectivity ($Z_{copol,total}$ [mm^6 m^{-3}]) which is the sum of the contributions from all
242 of the hydrometeor species.
243
244 **4 Sensor Capability Simulator**
245
246 In the previous section, total backscattered power resulting from all modeled hydrometeor species
247 (without any filtering) is estimated. In order to objectively assess model hydrometeor properties, they must
248 be converted to quantities that are comparable to observations, necessitating incorporation of sensor
249 detection limitations, including attenuation and finite sensitivity. Fortunately, lidar and radar sensors are
250 often relatively well-characterized so that sensor detection capabilities can be quantified and replicated in
251 forward-simulators for an objective model-to-observation comparison.
252
253 **4.1 Lidar Detection Capability**
254
255 Following the work of Cesana and Chepfer (2013), the (GO)^2-SIM lidar forward-simulator takes into
256 consideration that lidar power is attenuated by clouds. Attenuation is related to cloud optical depth (τ),
257 which is a function of total cloud extinction ($\sigma_{copol,total}$ [m^{-1}]) that includes the effect of cloud liquid
258 water and cloud ice via:
259
260 $$\tau = \int_{z0}^{z} \sigma_{copol,total} dh , \qquad (21)$$
261
262 Lidar attenuation is exponential and two-way as it affects the lidar power on its way out and back:
263
264 $$\beta_{copol,total,att} = \beta_{copol,total}\, e^{-2\tau}. \qquad (22)$$
265
266 In the current simulator we assume that only cloud segments with optical depth smaller than three can be
267 penetrated, other clouds being opaque (Cesana and Chepfer, 2013) such that total co-polar backscattered
268 power detected ($\beta_{copol,total,detect}$) is:
269
270 $$\beta_{copol,total,detect} = \beta_{copol,total,att} \quad \text{where } \tau \leq 3;$$
271 $$\beta_{copol,total,detect} = \text{undetected} \quad \text{where } \tau > 3. \qquad (23)$$
272
273 For the sample ModelE output shown in Fig. 2, Fig. 4a illustrates results from the lidar forward-simulator
274 for one forward-ensemble member (i.e., using a single set of lidar backscattered power empirical
275 relationships specifically eqns. (1) and (4)). Figure 4a$_1$ shows lidar total co-polar backscattered power
276 without consideration of sensor limitations, such as attenuation, which are included in Fig. 4a$_2$. Lidar
277 attenuation prevents the tops of deep systems containing supercooled water layers from being observed

278   (e.g., magenta boxes on 08/10 and 08/13). For the one-year sample the forward-simulated lidar system
279   detects only 35.5% of simulated hydrometeor-containing grid cells. In Sec. 6 we will determine which
280   hydrometeors (liquid water or ice) are responsible for the detected signals.

281

282   **4.2 Radar Detection Capability**

283

284   Millimeter-wavelength radars are also affected by signal attenuation. Radar signal attenuation depends
285   both on the transmitted wavelength and on the mass and phase of the hydrometeors. Liquid phase
286   hydrometeors attenuate radar signals at all millimeter radar wavelengths, even leading to total signal loss in
287   heavy rain conditions. In contrast, water vapor attenuation is less important at relatively longer wavelengths
288   (e.g., 8.56 mm; the wavelength simulated here) but can be important near wavelengths of 3.19 mm (the
289   CloudSat operating wavelength; (Bodas-Salcedo et al., 2011)).

290

291   At 8.56 mm (Ka-band) total co-polar attenuated reflectivity ($Z_{copol,total,att}$ [dBZ]) is given by

292

293    $Z_{copol,total,att} = Z_{copol,total} - a_{cl+pl},$ (24a)

294

295   where two-way liquid attenuation (a_{cl+pl} [dB]) is estimated using cloud and precipitating liquid water
296   contents (WC_{cl} and WC_{pl} [g m^{-3}]) and the thickness of the liquid layer (dh [m]):

297

298    $a_{cl+pl} = 2 \int_{z=0}^{z} [0.6 (WC_{pl} + WC_{cl})] dh.$ (24b)

299

300   In addition to attenuation, radars suffer from having a finite sensitivity that decreases with distance. Given
301   this, the total co-polar reflectivity detectable ($Z_{copol,total,detect}$ [dBZ]) is

302

303    $Z_{copol,total,detect} = Z_{copol,total,att}$ where $Z_{copol,total,att} \geq Z_{min},$
304    $Z_{copol,total,detect} = $ Undetected   where $Z_{copol,total,att} < Z_{min},$ (25a)

305

306   where the radar minimum detectable signal (Z_{min} [dBZ]) is a function of height (h [km]) and can be
307   expressed as
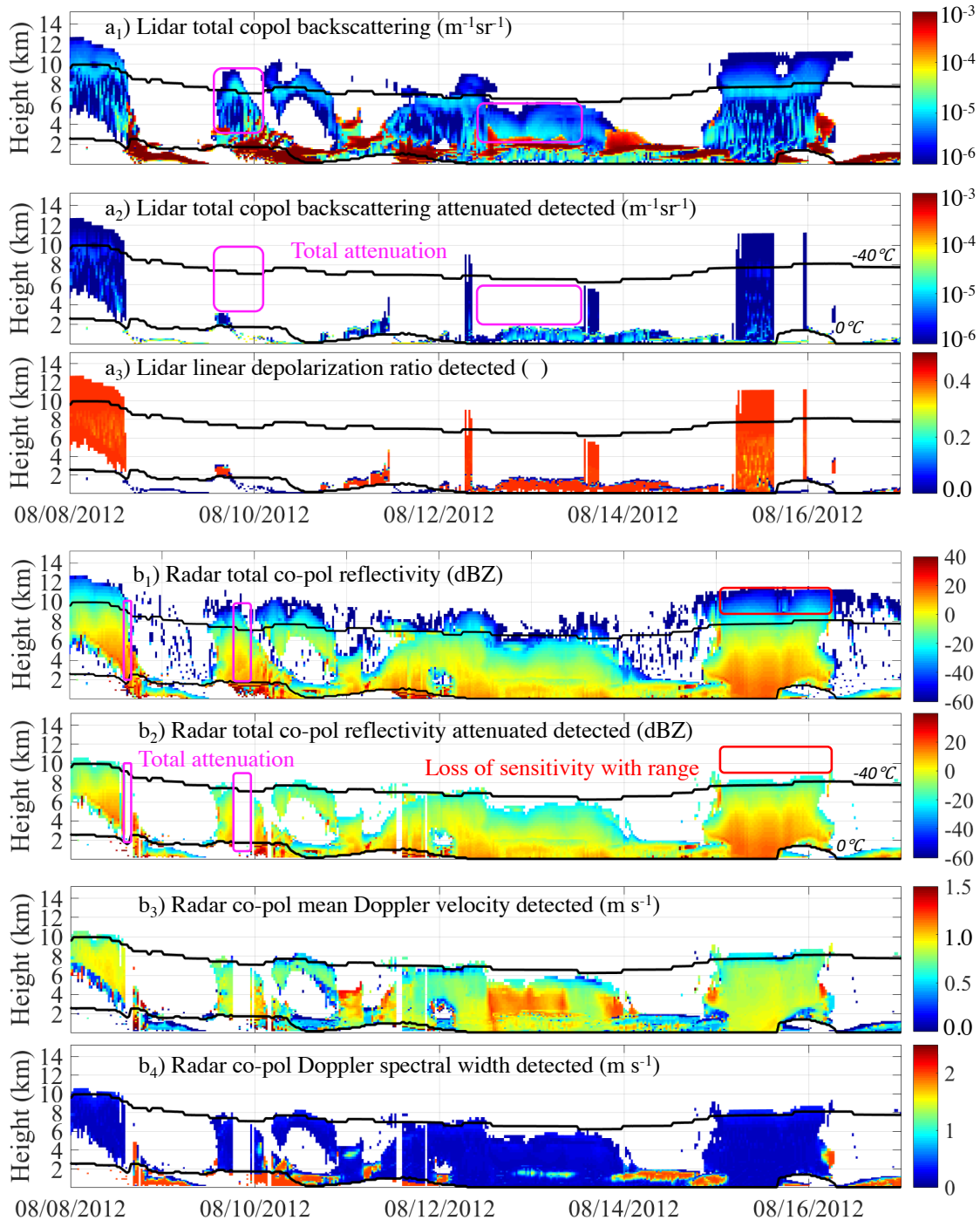
308

309    $Z_{min} = Z_{sensitivity\ at\ 1\ km} + 20 \log_{10} h.$ (25b)

310

311   A value of $Z_{sensitivity\ at\ 1\ km} = $ -41 dBZ is selected to reflect the sensitivity of the Ka-band ARM Zenith
312   Radar (KAZR) currently installed at the Atmospheric Radiation Measurement (ARM) North Slope of
313   Alaska observatory. This value has been determined by monitoring two years of observations and it reflects
314   the minimum signal observed at a height of 1 km. The minimum detectable signal used in the simulator
315   should reflect the sensitivity of the sensor used to produce the observational benchmark to be compared to
316   the forward-simulator output.

317

318   For the sample ModelE output shown in Fig. 2, Figure 4b illustrates results from the radar forward-
319   simulator for one forward-ensemble member (i.e., using a single set of radar reflectivity empirical
320   relationships specifically eqns. (9), (11a), (15) and (11b)). Figure 4b$_1$ shows radar total co-polar reflectivity
321   without consideration of sensor limitations, while Fig. 4b$_2$ includes the effects of attenuation and the range-
322   dependent minimum detectable signal. Sensor limitations make it such that heavy rain producing systems
323   cannot be penetrated (e.g., magenta box on 08/08 and 08/10) and the tops of deep systems cannot be
324   observed (e.g., red box on 08/15). For the one-year sample the forward-simulated radar system could detect
325   only 69.9 % of the simulated hydrometeor-containing grid cells. In Sec. 6 we will determine the phase of
326   the hydrometeors responsible for the detected signals.

Figure 4. Example outputs from the (GO)²-SIM backscattered power modules (1), sensor capability modules (2) and specialized-observables modules (3-4) for a) lidars and b) radars obtained using one set of empirical backscattered power relationships. This figure highlights sensor limitations ranging from attenuation (magenta boxes) to sensitivity loss with range (red boxes). Also indicated are the locations of the 0 °C and -40 °C isotherms (black lines). Note that positive velocities indicate falling motion.

4.3 Lidar-Radar Complementarity

Figures 4a$_2$ and 4b$_2$ highlight the complementarity of lidar and radar sensors. Despite sensor limitations, 532 nm lidar measurements can be used to characterize hydrometeors near the surface and infer the location of a lowermost liquid layer if one exists. In contrast, 8.56 mm radars have the ability to penetrate cloud layers and light precipitation, allowing them to determine cloud boundary locations (e.g, Kollias et al., 2016). For the one-year sample ModelE output the combination of both sensors enables detection of 73.0 % of the hydrometeor-containing grid cells. Real observations can be used to objectively evaluate these detectable hydrometeor populations while nothing can be said about those that are not detectable. Note that a number of undetectable grid cells only contain trace amounts of hydrometeors, which could be the result of numerical noise. As such the approach of considering sensor detection limitations helps objectively remove numerical noise from consideration and allows model and observations to converge towards a common hydrometeor definition for a fair comparison.

5 Forward Simulation of Specialized Observables

In the previous section total co-polar backscattered powers are used to determine which simulated hydrometeors are present in sufficient amounts to be detectable by sensors hence removing numerical noise from consideration. However, determining the phase of the detectable hydrometeor populations can be achieved with much greater accuracy by using additional observables.

Backscattered power alone provides a sense of hydrometeor number concentration (from lidar) and hydrometeor size (from radar), but it does not contain information about hydrometeor shape nor does it provide any hint on the number of coexisting hydrometeor species, both of which are relevant for phase determination. However, such information is available from lidar depolarization ratios and radar Doppler spectral widths.

5.1 Lidar Depolarization Ratio Simulator

So far we have described how hydrometeors of all types and phases affect co-polar radiation. It is important to note that radiation also has a cross-polar component which is only affected by nonspherical particles. Ice particles, which tend to be nonspherical, are expected to affect this component while we assume that cloud droplets, which tend to be spherical, do not. Taking the ratio of cross-polar to co-polar backscattering thus provides information about the dominance of ice particles in a hydrometeor population. This ratio is referred to as the linear depolarization ratio (δ_{detect}) and it can be estimated where hydrometeors are detected by the lidar.

$$\delta_{\text{detect}} = \frac{\beta_{\text{crosspol,ci,detect}}}{\beta_{\text{copol,total,detect}}}. \tag{26a}$$

According to Cesana and Chepfer (2013) analysis of CALIPSO observations, cloud ice particle cross-polar backscattering ($\beta_{\text{crosspol,detect}}$ [m^{-1}sr^{-1}]) can be approximated using the following relationship:

$$\beta_{\text{crosspol,ci,detect}} = \frac{0.29}{1-0.29}\,\beta_{\text{copol,ci,detect}}. \tag{26b}$$

For the sample ModelE output shown in Fig. 2, Fig. 4a$_3$ shows an example of forward-simulated lidar linear depolarization ratios estimated using one set of backscattered power empirical relationships.

Geoscientific
Model Development
Discussions

Open Access

5.2 Radar Doppler Moment Simulator

Specialty Doppler radars have the capability to provide information about the movement of hydrometeors in the radar observation volume. This information comes in the form of the radar Doppler spectrum, which describes how backscattered power is distributed as a function of hydrometeor velocity (Kollias et al., 2011). The zeroth moment of the Doppler spectral distribution (the spectral integral) is radar reflectivity, the first moment (the spectral mean) is mean Doppler velocity (VD) and the second moment (the spectral spread) is Doppler spectral width (SW). Rich information is provided by the velocity spread (i.e., SW) of the hydrometeor population including information regarding the number of coexisting species, turbulence intensity and spread of the hydrometeor particle size distributions. Typically, the effects of turbulence and hydrometeor size variations on the velocity spread for a single species are much smaller than the effect of mixed-phase conditions. As such, Doppler spectral width is a useful parameter for hydrometeor phase identification.

Forward-simulations of Doppler quantities have been performed for cloud models using bin microphysics (e.g., Tatarevic and Kollias, 2015) but not, to our knowledge, for GCMs using 2-moment microphysics schemes. Co-polar mean Doppler velocity and co-polar Doppler spectral width are subject to the same detection limitations as radar reflectivity. In fact, just like radar reflectivity, these observables are strongly influenced by large hydrometeors; that is, they are reflectivity-weighted velocity averages.

Our approach begins by quantifying the contribution of each species present (P_{species}), which is determined by the species detected co-polar reflectivity ($Z_{\text{copol,species,detect}}$ [$\text{mm}^6\,\text{m}^{-3}$]) relative to the total detected co-polar reflectivity ($Z_{\text{copol,total,detect}}$ [$\text{mm}^6\,\text{m}^{-3}$]):

$$P_{\text{species}} = \frac{Z_{\text{copol,species,detect}}}{Z_{\text{copol,total,detect}}}, \tag{27a}$$

together with

$$Z_{\text{copol,species,detect}} = Z_{\text{copol,species}} - a_{\text{cl+pl}}, \text{ where } Z_{\text{copol,total,att}} \geq Z_{\text{min}}. \tag{27b}$$

In Eqns. 27a-b the subscript "species" represents cl, ci, pl, or pi. Attenuation ($a_{\text{cl+pl}}$) and minimum detectable signal (Z_{min}) are as in Eq. 24. The mass-weighted fall velocity of each species (V_{species} [m s^{-1}]) is a GCM output and the total mean Doppler velocity detected ($\text{VD}_{\text{copol,detect}}$ [m s^{-1}]) is the sum of the reflectivity-weighted contribution of each species:

$$\text{VD}_{\text{copol,detect}} = P_{\text{cl}}V_{\text{cl}} + P_{\text{pl}}V_{\text{pl}} + P_{\text{ci}}V_{\text{ci}} + P_{\text{pi}}V_{\text{pi}}. \tag{28}$$

Total Doppler spectral width ($\text{SW}_{\text{copol,detect}}$ [m s^{-1}]) is more complex and combines hydrometeor species fall velocity (V_{species} [m s^{-1}]) and spectral width ($\text{SW}_{\text{species}}$ [m s^{-1}]) information:

$$\text{SW}_{\text{copol,detect}} =$$
$$P_{\text{cl}}\left(\text{SW}_{\text{cl}}^2 + \left(V_{\text{cl}} - \text{VD}_{\text{copol,detect}}\right)^2\right) + P_{\text{pl}}\left(\text{SW}_{\text{pl}}^2 + \left(V_{\text{pl}} - \text{VD}_{\text{copol,detect}}\right)^2\right) +$$
$$P_{\text{ci}}\left(\text{SW}_{\text{ci}}^2 + \left(V_{\text{ci}} - \text{VD}_{\text{copol,detect}}\right)^2\right) + P_{\text{pi}}\left(\text{SW}_{\text{pi}}^2 + \left(V_{\text{pi}} - \text{VD}_{\text{copol,detect}}\right)^2\right), \tag{29}$$

where the spectral widths of individual species are assigned climatological values. These climatological values are $\text{SW}_{\text{cl}} = 0.10\,\text{m s}^{-1}$, $\text{SW}_{\text{ci}} = 0.05\,\text{m s}^{-1}$, $\text{SW}_{\text{pi}} = 0.15\,\text{m s}^{-1}$ and $\text{SW}_{\text{pl}} = 2.00\,\text{m s}^{-1}$ (Kalesse et al., 2016).

427 For the sample ModelE output shown in Fig. 2, Figs. $4b_3$ and $4b_4$ respectively show examples of forward
428 simulated mean Doppler velocity and Doppler spectral width estimate using one set of empirical radar
429 reflectivity relationship.
430
6   Water Phase Classifier Algorithm
432
433   From a purely numerical modeling perspective the simplest approach to defining the phase of a
434 hydrometeor population contained in grid cells is to consider that any nonzero hydrometeor mixing ratio
435 species contributes to the phase of the population. Using this approach, in the one-year sample, we find that
436 the detectable hydrometeor-containing grid cells are 2.4 % pure liquid, 19.4 % pure ice and 78.2 % mixed
437 phase (Note how these water phase statistics differ by up to 18.4 % from Sec. 2 where all grid cells,
438 potentially including numerical noise, were considered). But determining hydrometeor phase in
439 observational space is not as straightforward. It is complicated by the fact that sensors do not record ice-
440 and liquid-hydrometeor returns separately but rather record total backscattering from all hydrometeors.
441 Retrieval algorithms are typically applied to the observed total backscattering to determine the phase of
442 hydrometeor populations. However, phase classification algorithms have limitations that require each
443 hydrometeor species to be present not only in nonzero amounts but in amounts sufficient to produce a
444 phase signal. Thus, hydrometeor phase statistics obtained from a numerical model in the absence of a
445 forward simulator are not necessarily comparable with equivalent statistics retrieved from observables,
446 especially in instances where one hydrometeor species dominates the grid cell and other species are present
447 in trace amounts. A common hydrometeor phase definition must be established to objectively evaluate the
448 phase of simulated hydrometeor populations using observations, which requires the development of a phase
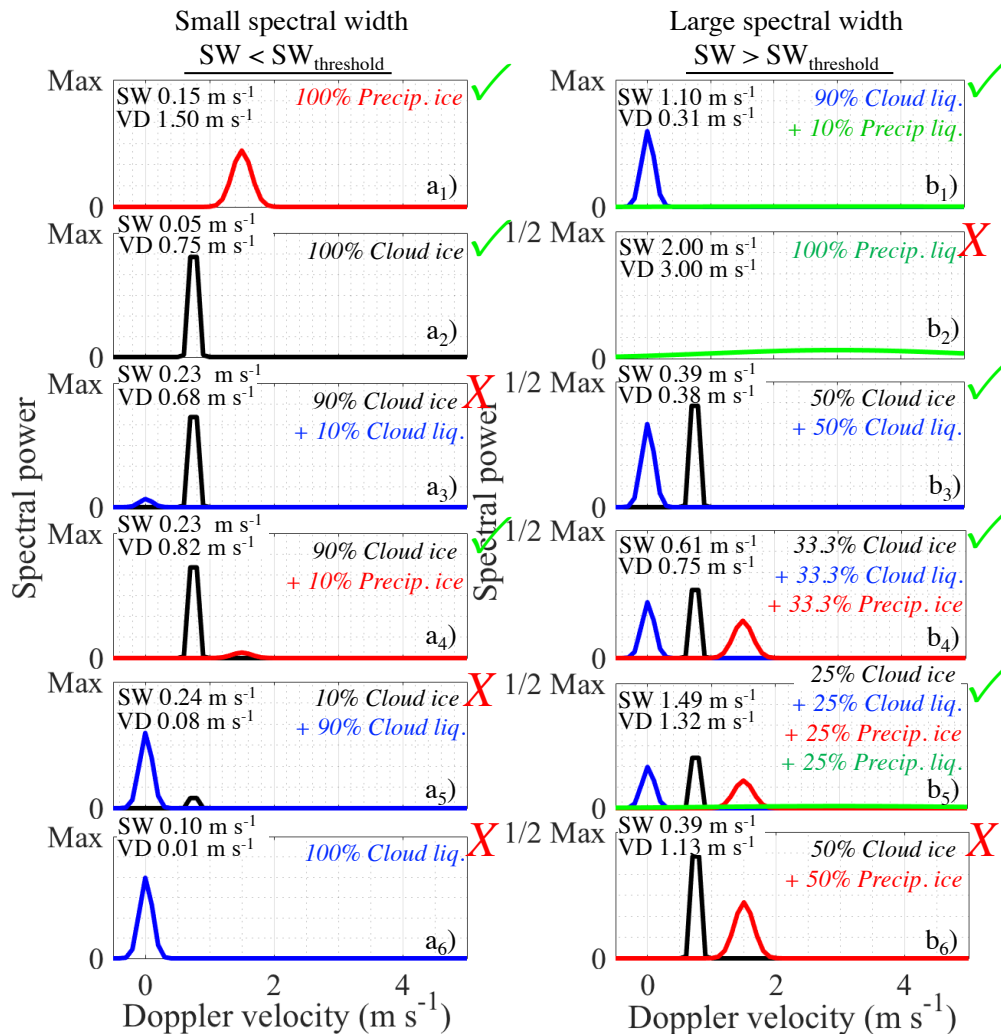449 classification algorithm that can be applied to observables both forward-simulated and real.
450
451 The scientific literature contains a number of phase classification algorithms with different levels of
452 complexity. Hogan et al. (2003) used regions of high lidar backscattered power as an indicator for the
453 presence of liquid droplets. Lidar backscattered power combined with lidar linear depolarization ratio has
454 been used to avoid some of the misclassifications encountered when using backscattered power alone (e.g.,
455 Yoshida et al., 2010; Hu et al., 2007a; Hu et al., 2009; Hu et al., 2010; Sassen, 1991). Hogan and O'Connor
456 (2004) proposed using lidar backscattered power in combination with radar reflectivity. While the
457 combination of radar and lidar backscattered powers is useful for the identification of mixed-phase
458 conditions, their combined extent remains limited to single layer clouds or to lower cloud decks because of
459 lidar signal attenuation. Shupe (2007) proposed a technique in which radar Doppler velocity information is
460 used as an alternative to lidar backscattering information (for ranges beyond that of lidar total attenuation)
461 to infer the presence of supercooled water in multi-layer systems. Figure 5 displays cartoons of Doppler
462 spectra that have the same total co-polar radar reflectivity but different total mean Doppler velocities (VD)
463 and Doppler spectral widths (SW) resulting from different hydrometeor species and combinations, thus
464 highlighting the added value of Doppler information. The contribution of each species to the total co-polar
465 reflectivity is indicated as a percentage in the top right of each subpanel. These scenarios show that VD
466 tends to be relatively small for pure liquid cloud (Fig. $5a_6$), pure ice cloud (Fig. $5a_2$), and even mixed-phase
467 non-precipitating cloud (Fig. $5a_3,a_5,b_3$) and only tends to increase when precipitation is present in cloud
468 (Fig. 5 a_4,b_3,b_4,b_5) or below cloud (Fig. $5a_1,b_2$), making VD a seemingly robust indicator for precipitation
469 occurrence but not for phase identification. These scenarios also show that SW tends to be relatively small
470 in single-phase clouds without precipitation (Fig. $5a_2,a_6$), pure precipitating ice (Fig. $5a_1$) and multi-species
471 clouds with a dominant hydrometeor species (Fig. $5a_3,a_5$). On the other hand, SW tends to be large when
472 liquid precipitation is present (Fig. $5b_1,b_2,b_5$) and in mixed-phase clouds without a dominant species (Fig.
473 $5b_3,b_4,b_5$). These scenarios suggest that large spectral widths are useful indicators for the presence of
474 supercooled rain and mixed-phase conditions. Scenarios where this interpretation of spectrum width is
475 incorrect will be discussed in Sec. 6.3.
476

Geoscientific
Model Development
Discussions

477 Regardless of which observation they are based-on, the aforementioned phase classification schemes all
478 rely on assumption that hydrometeor phases when projected on observational space (e.g., lidar
479 backscattered power against lidar depolarization ratio) create well-defined patterns that can be separated
480 using thresholds.
481
482

483
484
485 **Figure 5.** Cartoon examples of radar Doppler spectra from different hydrometeors combinations:
486 precipitating ice (red), cloud ice (black), precipitating water (green) and cloud water (blue). The
487 contribution of each hydrometeor species to the total co-polar reflectivity is indicated in the top right of
488 each subpanel. Each radar Doppler spectrum has been normalized to have the same total co-polar radar
489 reflectivity which highlights that different hydrometeor combinations generate unique mean Doppler
490 velocity (VD) and Doppler spectral width (SW) signatures. As discussed in Sec. 6, low spectral width
491 signatures are assumed to be associated with ice conditions (column a) while high spectral width signatures
492 are assumed to associated with liquid/mixed-phase conditions (column b). Hydrometeor combinations that
493 respect these assumptions are marked with √-marks. Exceptions to these rules (X-marks) are responsible
494 for $(GO)^2$-SIM phase misclassifications above the level of lidar extinction. This list is not exhaustive.

6.1 Observational Thresholds for Hydrometeor Phase Identification

While the thresholds used for the radar reflectivity, lidar backscattered power, and lidar depolarization ratio are generally accepted by the remote sensing community, the same cannot be said about the radar Doppler velocity and Doppler spectral width thresholds suggested by Shupe (2007). The (GO)^2-SIM framework allows us to evaluate and/or adjust these thresholds because simulated mixing ratios of liquid and ice hydrometeors are known. The use of all such thresholds for phase classification is evaluated using joint frequency of occurrence histograms of hydrometeor mixing ratios for a single species and forward-simulated observable values (resulting from all hydrometeor types; Fig. 6). This exercise is repeated for each forward-simulation of the ensemble in order to provide a measure of uncertainty and ensure that the choice of empirical relationship does not affect our conclusions.

As one example, the joint frequency of occurrence histogram of lidar total co-polar backscattered power ($\beta_{copol,total,detect}$) and cloud liquid mixing ratio is plotted with the objective of isolating cloud ice particles from cloud water droplets (Fig. 6a$_1$, black contour lines). Two distinct clusters are evident in the joint histogram in Fig. 6a$_1$: 1) $\beta_{copol,total,detect}$ between $10^{-6.7}$ m^{-1}sr^{-1} and $10^{-5.1}$ m^{-1}sr^{-1} for cloud liquid water mixing ratios between $10^{-10.6}$ kg kg^{-1} and $10^{-8.8}$ kg kg^{-1} which we conclude result primarily from cloud ice particle contributions, and 2) $\beta_{copol,total,detect}$ between $10^{-4.6}$ m^{-1}sr^{-1} and $10^{-3.8}$ m^{-1}sr^{-1} for cloud liquid water mixing ratios between $10^{-6.4}$ kg kg^{-1} and $10^{-4.3}$ kg kg^{-1} which we conclude result primarily from cloud liquid droplet contributions. Therefore, a threshold for best distinguishing these two distinct populations should lie somewhere between $10^{-5.1}$ m^{-1}sr^{-1} and $10^{-4.6}$ m^{-1}sr^{-1}.

To objectively determine an appropriate threshold to separate different hydrometeor populations, we start by normalizing the joint histogram of mixing ratio values for fixed ranges of observable values of interest. This normalization is done by assigning a value of 1 to the frequency of occurrence of the most frequently occurring mixing ratio value per observable range. It is then possible to evaluate the change of this most frequently occurring mixing ratio as a function of observable value. The observable value that intersects the largest change in most frequently occurring mixing ratio is then set as the threshold value.
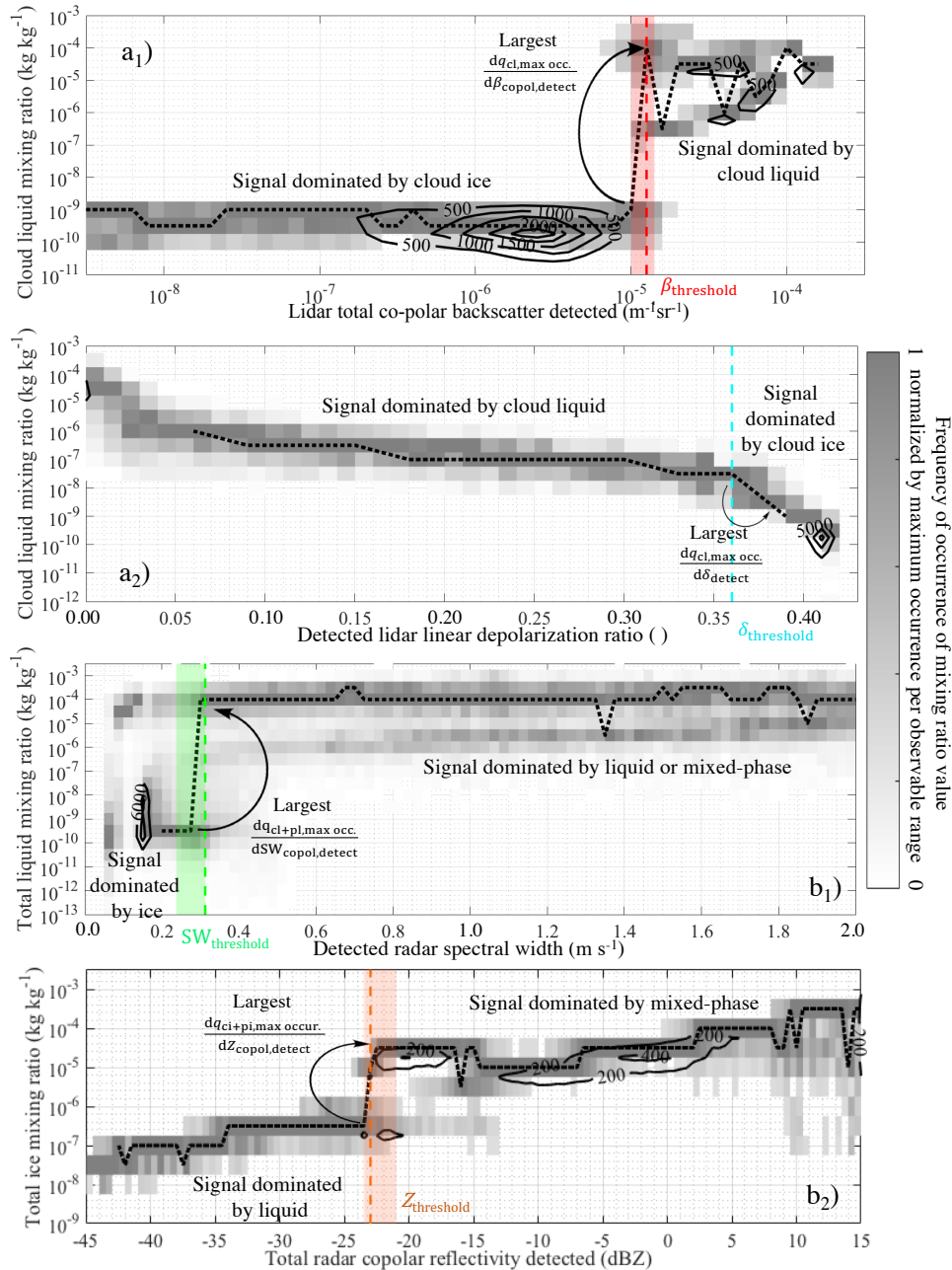
In the example presented in Fig. 6a$_1$, the darkest grey shading is indicative of the most frequency occurring cloud liquid mixing ratio for each lidar backscattered power range. The dotted black line in Fig. 6a$_1$ connects these most frequently occurring mixing ratio values. A curved arrow points to the largest change in most frequently occurring mixing ratio as a function of $\beta_{copol,total,detect}$. A red dashed line at $10^{-4.9}$ m^{-1}sr^{-1} indicates the lidar backscatter value that intersects this largest change in mixing ratio and represents an objective threshold value for this example forward-simulation. As mentioned earlier, this threshold is expected to change with the choice of empirical relationships used in the forward simulator. For the 576 forward-simulator realizations of this version of ModelE outputs, the interquartile range of $\beta_{copol,total,detect}$ threshold values ranged from 10^{-5} m^{-1}sr^{-1} to $10^{-4.85}$ m^{-1}sr^{-1} (red shaded vertical column).

The different panels in Fig. 6 show that similar observational patterns occur in the water mixing ratio versus lidar or radar observable histograms such that objective thresholds for hydrometeor phase classification can be determined for all of them. The second threshold determined is for the detected lidar linear depolarization (δ_{detect}), once again with the goal of separating returns dominated by cloud droplets versus cloud ice particles (Fig. 6a$_2$). If we first identify the model grid cells with backscattered power above the lidar detectability threshold of 10^{-6} m^{-1}sr^{-1}, the threshold to distinguish between ice particles and liquid droplets is 0.36 (cyan dashed line). In the 576 forward realizations from this version of ModelE this threshold is stable at 0.36. Note that this threshold is not allowed to fall below 0.05 m s^{-1}.

Geoscientific
Model Development
Discussions
Open Access
EGU

Figure 6. Example of joint frequency of occurrence histograms (contours) and normalized subsets from the joint histograms (grey shading) for one (GO)^2-SIM forward-realization: a$_1$) $\beta_{copol,total,detect}$, a$_2$) δ_{detect}, b$_1$) SW$_{copol,detect}$, and b$_2$) $Z_{copol,total,detect}$. These are used for the determination of objective water phase classifier thresholds (vertical colored dashed lines) that are set at the observational value with the largest change (see curved arrows) in most frequently occurring mixing ratio. These thresholds are not fixed but rather re-estimated for each forward-ensemble member. The widths of the color shaded vertical columns represent the interquartile range spreads generated from 576 different forward-realizations.

Geoscientific
Model Development
Discussions

551 The third threshold determined is the radar detected co-polar spectral width ($SW_{copol,detect}$) value that
552 separates ice dominated from liquid/mixed-phase dominated returns (Fig. 6b$_1$). We isolate the model grid
553 cells with sub-zero temperatures and look for the most appropriate $SW_{copol,detect}$ threshold between 0.2 m s^{-1}
554 and 0.5 m s^{-1} to isolate the ice population. For the example forward-simulation we find a threshold of 0.31
555 m s^{-1} (green dashed line), and over all forward-realizations this threshold ranges from 0.24 m s^{-1} to 0.31 m
556 s^{-1} (green shaded vertical column).

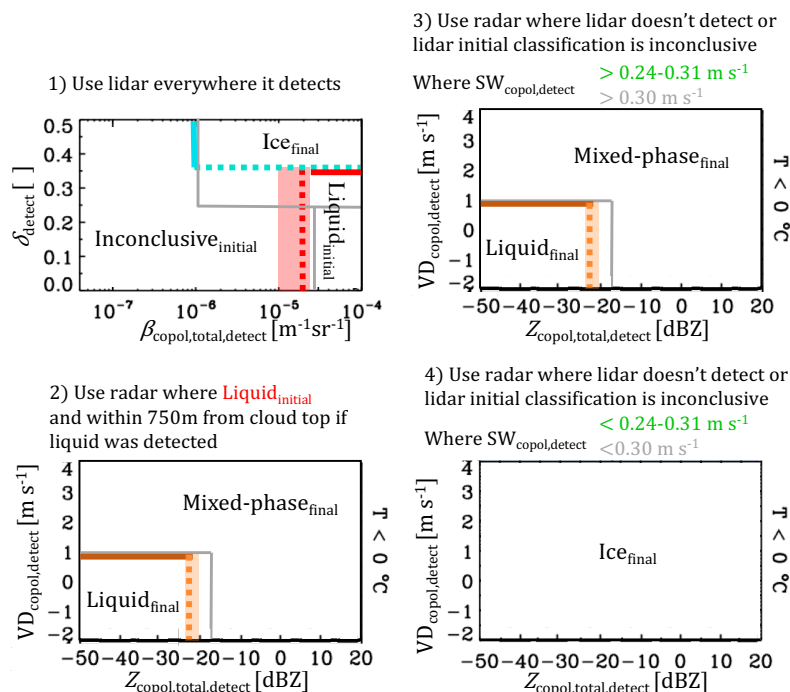558 The last threshold determined is the radar total co-polar reflectivity detected ($Z_{copol,total,detect}$) value that
559 separates liquid from mixed-phase dominated returns (Fig. 6b$_2$). If we isolate the model grid cells with sub-
560 zero temperatures, spectral widths within the liquid/mixed-phase range, and with mean Doppler velocities
561 smaller than 1 m s^{-1}, the threshold to distinguish between liquid and mixed-phase is objectively set to -23
562 dBZ (orange dashed line). This threshold ranges from -23.5 dBZ to -21.0 dBZ over the 576 forward
563 realizations obtained from this version of ModelE outputs (orange shaded vertical column).

565 The objectively determined thresholds optimize the performance of the hydrometeor phase classification
566 algorithm and are expected to generate the best (by minimizing false detection) hydrometeor phase
567 classifications. Results using these flexible thresholds are compared in Sec. 6.3 to results using the fixed
568 empirical thresholds of Shupe (2007).

570 **6.2 Hydrometeor Phase Map Generation**

572 Hydrometeor phase maps are produced for each forward realization by applying the objectively
573 determined flexible thresholds or fixed thresholds modified from Shupe (2007) as illustrated in Fig. 7.
574

576 **Figure 7.** Collective illustration of hydrometeor phase classification thresholds and phase classification
577 sequence. Fixed thresholds modified from Shupe (2007) are displayed as grey lines. The objectively
578 determined flexible thresholds are displayed using dashed colored lines and colored shading as in Fig. 6.
579 Note that positive velocities indicate downward motion.

Geoscientific
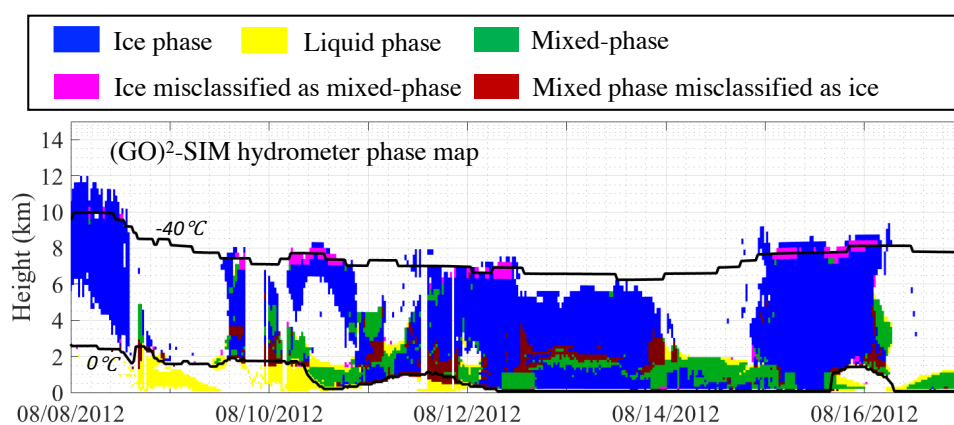Model Development
Discussions

580 Thresholds are applied in sequence. Where the lidar signal is detected it is used for initial classification of
581 liquid-dominated grid cells (Fig. 7.1, red box) and final classification of ice-dominated grid cells (Fig. 7.1,
582 cyan box). Grid cells initially classified as containing liquid drops by the lidar are subsequently reclassified
583 as either liquid dominated (Fig. 7.2, orange box) or mixed-phase (Fig. 7.2, outside of orange box) by the
584 radar which is more sensitive to the larger ice particles. Because studies suggest that supercooled water
585 layers extend to the tops of shallow clouds, if liquid containing grid cells were identified within 750 m of
586 cloud top, the radar is used to determine if there are other liquid or mixed-phase hydrometeor populations
587 from the range of lidar attenuation to cloud top (Fig.7.2; and just as in Shupe (2007)). Hydrometeor-
588 containing grid cells either not detected by the lidar or whose initial phase classification is inconclusive
589 (Fig. 7.1, inconclusive region) are subsequently classified using their radar moments. If radar spectral width
590 is above the threshold grid cells are finally classified as liquid (Fig.7.3, orange box) or mixed-phase (Fig.
591 7.3, outside the orange box) depending on their other radar moments. If radar spectral width is below the
592 threshold grid cells are finally classified as ice phase (Fig. 7.4). As a final step detected hydrometeors in
593 grid cells at temperatures above 0 °C are reclassified to liquid phase while those at temperatures below -40
594 °C are reclassified to the ice phase.

596 Figure 8 shows an example of (GO)^2-SIM water phase classification for one forward-ensemble member
597 using objectively determined thresholds. During the first day of this example simulation, ModelE produced
598 what appears to be a thick cirrus. The simulator classified this cirrus as mostly ice phase (blue). The
599 following day of 08/09, ModelE generated enough hydrometeors to attenuate both the forward-simulated
600 lidar and radar signals. The algorithm identified these hydrometeors as liquid phase (yellow). For the
601 following few days (08/11-08/14) deep hydrometeor systems extending from the surface to about 8 km
602 were produced. According to (GO)^2-SIM they were mostly made up of ice-phase particles (blue) with two
603 to three shallow mixed-phase layers at 2 km, 4 km and 7 km. Finally, on 08/14 hydrometeor systems appear
604 to become shallower (2-km altitudes) and liquid topped (yellow). For the entire one-year simulation, of the
605 333,927 detectable hydrometeor-containing grid cells, the phase classifier applied to our example forward-
606 simulation ensemble member identified 12.2 % pure-liquid, 68.7 % pure-ice and 19.1 % mixed-phase

Figure 8. Example output from (GO)^2-SIM phase-classification algorithms (using objectively determined thresholds and one set of empirical relationships in the forward-simulator). The locations of ice-phase hydrometeors (blue), liquid-phase hydrometeors (yellow) and mixed-phase hydrometeors (green) are illustrated. After evaluation against the original ModelE output mixing-ratios, we found that some mixed-phase hydrometeors were misclassified as ice phase (red) and some ice-phase hydrometeors were misclassified as mixed phase (magenta). Also indicated are the locations of the 0 °C and -40 °C isotherms (black lines).

Geoscientific
Model Development
Discussions

Open Access

617 conditions. Hydrometeor phase statistics estimated using this objective definition of hydrometeor phase
618 differ by up to 60 % from those discussed at the beginning of this section that were simply based on model
619 output nonzero mixing ratios. This indicates that a large number of grid cells containing detectable
620 hydrometeor populations were dominated by one species and that the amounts of the other species were too
621 small to create a phase classification signal. This highlights the need to create a framework that both
622 objectively identifies grid cells containing detectable hydrometeors populations and determines the phase
623 of the hydrometeors dominating them using a phase classification technique consistent with observations.
624
625 **6.3 Phase Classification Algorithm Limitations**
626
627 Hydrometeor-phase classification evaluation is facilitated in the context of forward-simulators
628 because inputs (i.e., model-defined hydrometeor phase) are known. Model mixing-ratios are used to check
629 for incorrect hydrometeor phase classifications over the entire forward-realization ensemble (Table 1b).
630
631 Without any ambiguity, it is possible to identify false-positive phase classifications (Table 1b). A false-
632 positive phase classification occurs when a grid cell containing 0 kg kg^{-1} of ice particles (liquid drops) is
633 wrongly classified as ice or mixed phase (liquid or mixed phase). In this study a negligible number (0.5 %)
634 of hydrometeor-containing model grid cells are wrongly classified as containing liquid. Similarly, a
635 negligible number (~0.0 %) of hydrometeor-containing model grid cells are wrongly classified as
636 containing ice particles, whereas 1.1 % of pure liquid- or ice-containing model grid cells are wrongly
637 classified as mixed-phase. Using model mixing ratios, it is possible to determine the appropriate phase of
638 these false-positive classifications ("False negative" row in Table 1b). An additional 1.5 % of all
639 hydrometeor-containing model grid cells should be classified as ice phase while a negligible number (0.2
640 %) of liquid water is missed.
641
642 Quantifying the number of mixed-phase false negatives (i.e., the number of grid cells that should have
643 been, but were not, classified as mixed-phase) is not as straightforward because it requires us to define
644 mixed-phase conditions in model space. For a rough estimate of mixed-phase false negatives we check if
645 model grid cells classified as containing a single phase contained large amounts of hydrometeors of other
646 phase types, with large amount being defined here as a mixing-ratio greater than 10^{-5} kg kg^{-1}. This mixing-
647 ratio amount was chosen because it is associated with noticeable changes in observables, as seen in Fig. 6.
648 Using this mixed-phase definition, we find that 1.4 % of liquid-only classified grid cells contained large
649 amounts of ice particles and 3.8 % of ice-only classified grid cells contained large amounts of liquid
650 ("Questionable" row in Table 1b). Everything considered, only 6.9 % of model grid cells with detectable
651 hydrometeor populations were misclassified according to their phase.
652
653 For completeness we examined the circumstances associated with the most frequent phase-classification
654 errors. Most of these errors occurred above the altitude at which the lidar beam was completely attenuated,
655 where only radar spectral widths are used to separate liquid/mixed-phase hydrometeors from ice-phase
656 hydrometeors.
657
658 The first set of phase-classifier errors was a scarcity of pure ice particles (1.5 % false-negative ice phase).
659 In the current (GO)^2-SIM implementation, ice particle populations are sometimes incorrectly classified as
660 liquid/mixed-phase populations where cloud ice and precipitating ice hydrometeors coexist. This happens
661 because mixtures of cloud and precipitating ice particles sometimes generate large Doppler spectral widths
662 similar to those of mixed-phase clouds (Fig. 5b$_6$). In this example simulation ModelE produced such
663 mixtures close to the -40 °C isotherm near the tops of deep cloud systems (e.g., Fig. 8, 08/15 around 8 km;
664 magenta).
665

Geoscientific
Model Development
Discussions

666 In contrast, mixed-phase conditions were sometimes misclassified as pure ice (3.8 %; "Questionable" row
667 in Table 1b). This occurred when large amounts of liquid drops coexisted with small amounts of ice
668 particles that generated small spectral widths incorrectly associated with pure ice particles (Fig. 5a$_5$). In this
669 example simulation, ModelE produced such conditions just above the altitude of lidar beam extinction in
670 cloud layers with ice falling into supercooled water layers (e.g., Fig. 8, 08/13 around 3 km; red).

672 Other possible misclassification scenarios associated with spectral width retrievals are presented in Fig. 5
673 and identified with the red X-marks. These other misclassification scenarios are not responsible for large
674 misclassification errors here but could be in other simulations. As such, (GO)^2-SIM errors should be
675 quantified every time it is applied to a new region or numerical model.

6.4 Sensitivity on the Choice of Threshold

679 The performance of the objectively determined flexible phase-classification thresholds (illustrated
680 using colored dashed lines and shading in Fig. 7) is examined against those proposed by Shupe (2007) with
681 one exception (illustrated using grey lines in Fig. 7). The modification to Shupe (2007) is that radar
682 reflectivity larger than 5 dBZ are not associated with the snow category since introducing this assumption
683 was found to increase hydrometeor-phase misclassification (not shown). From Fig. 7 it is apparent that both
684 sets of thresholds are very similar. We estimate that hydrometeor phase frequency of occurrence produced
685 by both threshold sets are within 6.1 % of each other and that the fixed thresholds modified from Shupe
686 (2007) only produce phase misclassification in an additional 0.7 % of hydrometeor-containing grid cells
687 (compare Table 1b to Table 1c). These results suggest that the use of lidar-radar threshold-based techniques
688 for hydrometeor-phase classification depends little on the choice of thresholds.

7 An Ensemble Approach for Uncertainty Quantification

692 Owing to the limited information content in models with regard to detailed particle property
693 information, all forward simulators must rely on a set of assumptions to estimate hydrometeor
694 backscattered power. (GO)^2-SIM performs an uncertainty assessment by performing an ensemble of 576
695 forward simulations based on 18 different empirical relationships (relationships are listed in Table 2). The
696 spread generated by these different combinations is expressed using median values and interquartile ranges
697 (IQR; Table 1b,c). The fact that the largest interquartile range is 3.7 % suggests that the number of grid
698 cells containing detectable hydrometeors as well as hydrometeor phase statistics estimated using the
699 proposed lidar-radar algorithm are rather independent of backscattered power assumptions in the forward
700 simulator. Nevertheless, we suggest using the full range of frequency of occurrences presented in Tables
701 1b,c for future model evaluation using observations.

8 Summary and Conclusions

705 Ground-based active remote sensors offer a favorable perspective for the study of shallow and
706 multi-layer mixed-phase clouds because ground-based sensors are able to collect high resolution
707 observations close to the surface where supercooled water layers are expected to be found. In addition,
708 ground-based sensors have the unique capability to collect Doppler velocity information that has the
709 potential to help identify mixed-phase conditions even in multi-layer cloud systems.

711 Because of differences in hydrometeor and phase definitions, among other things, observations remain
712 incomplete benchmarks for general circulation model (GCM) evaluation. Here, a GCM-oriented ground-
713 based observation forward-simulator [(GO)^2-SIM] framework for hydrometeor-phase evaluation is
714 presented. This framework bridges the gap between observations and GCMs by mimicking observations

Geoscientific
Model Development
Discussions

715 and their limitations and producing hydrometeor-phase maps with comparable hydrometeor definitions and
716 uncertainties.
717
718 Here, results over the North Slope of Alaska extracted from a one-year global ModelE (current
719 development version) simulation are used as an example. (GO)^2-SIM uses as input native resolution GCM
720 grid-average hydrometeor (cloud and precipitation, liquid and ice) area fractions, mixing ratios, mass-
721 weighted fall speeds and effective radii. These variables offer a balance between those most essential for
722 forward simulation of observed hydrometeor backscattering and those likely to be available from a range of
723 GCMs going forward, making (GO)^2-SIM a portable tool for model evaluation. (GO)^2-SIM outputs
724 statistics from 576 forward-simulation ensemble members all based on a different combination of eighteen
725 empirical relationships that relate simulated water content to hydrometeor backscattered power as would be
726 observed by vertically pointing micropulse lidar and Ka-band radar; The interquartile range of these
727 statistics being used as an uncertainty measure.
728
729 (GO)^2-SIM objectively determines which hydrometeor-containing model grid cells can be assessed based
730 on sensor capabilities, bypassing the need to arbitrarily filter trace amounts of simulated hydrometeor
731 mixing ratios that may be unphysical or just numerical noise. Limitations that affect sensor capabilities
732 represented in (GO)^2-SIM include attenuation and range dependent sensitivity. In this approach 78.3 % of
733 simulated grid cells containing nonzero hydrometeor mixing ratios were detectable and can be evaluated
734 using real observations, with the rest falling below the detection capability of the forward-simulated lidar
735 and radar leaving them unevaluated. This shows that comparing all hydrometeors produced by models with
736 those detected by sensors would lead to inconsistencies in the evaluation of quantities as simple as cloud
737 and precipitation locations and fraction.
738
739 While information can be gained from comparing the forward-simulated and observed fields, hydrometeor-
740 phase evaluation remains challenging owing to inconsistencies in hydrometeor-phase definitions. Models
741 evolve ice and liquid water species separately such that their frequency of occurrence can easily be
742 estimated. However, sensors record information from all hydrometeor species within a grid cell without
743 distinction between signals originating from ice particles or liquid drops. The additional observables of
744 lidar linear depolarization ratio and radar mean Doppler velocity and spectral width are forward simulated
745 to retrieve hydrometeor phase. The results presented here strengthen the idea that hydrometeor-phase
746 characteristics lead to distinct signatures in lidar and radar observables, including the radar Doppler
747 moments which have not been evaluated previously. Our analysis confirms that distinct patterns in
748 observational space are related to hydrometeor phase and an objective technique to isolate liquid, mixed-
749 phase and ice conditions using simulated hydrometeor mixing ratios was presented. The thresholds
750 produced by this technique are close to those previously estimated using real observations, further
751 highlighting the robustness of thresholds for hydrometeor-phase classification.
752
753 The algorithm led to hydrometeor phase misclassification in no more than 6.9 % of the hydrometeor-
754 containing grid cells. Its main limitations were confined above the altitude of lidar total attenuation where it
755 sometimes failed to identify additional mixed-phase layers dominated by liquid water drops and with few
756 ice particles. Using the same hydrometeor-phase definition for forward-simulated observables and real
757 observations should produce hydrometeor-phase statistics with comparable uncertainties. Alternatively,
758 disregarding how hydrometeor phase is observationally retrieved would lead to discrepancies in
759 hydrometeor-phase frequency of occurrence up to 40 %, a difference attributable to methodological bias
760 and not to model error. So, while not equivalent to model "reality" a forward-simulator framework offers
761 the opportunity to compare simulated and observed hydrometeor-phase maps with similar limitations and
762 uncertainties for a fair model evaluation.
763

The next steps to GCM evaluation using ground-based observations include the creation of an artifact-free observational benchmark and addressing model and observation scale differences. While the (GO)^2-SIM modules presented here capture sensor limitations related to backscattered power attenuations, they do not account for sensitivity inconsistencies, clutter and insect contamination, all of which affect the observations collected by the real sensors. Only thorough evaluation of observational datasets and application of masking algorithms to them can remediate these issues. Several approaches, from the subsampling of GCMs to the creation of CFADs, have been proposed to address the scale difference. A follow-up study will describe how observational resampling in the context of the cloud vertical structure approach (Rémillard and Tselioudis, 2015) can be used to account for scale differences in the context of GCM hydrometeor-phase evaluation.

(GO)^2-SIM is a step towards creating a fair hydrometeor-phase comparison between GCM output and ground-based observations. Owing to its simplicity and robustness, (GO)^2-SIM is expected to help assist in model evaluation and development for models such as ModelE, specifically with respect to hydrometeor phase in shallow cloud systems.

Code Availability

The ModelE code used to produce the results presented here resides within the ModelE development repository and is available upon request from the corresponding author. Results here are based on ModelE tag modelE3_2017-06-14, which is not a publicly released version of ModelE but is available on the ModelE developer repository at https://simplex.giss.nasa.gov/cgi-bin/gitweb.cgi?p=modelE.git;a=tag;h=refs/tags/modelE3_2017-06-14. The (GO)^2-SIM modules described in the current manuscript can be fully reproduced using the information provided. Interested parties are encouraged to contact the corresponding author for additional information on how to interface their numerical model with (GO)^2-SIM.

References

Atlas, D.: The estimation of cloud parameters by radar, J. Meteorol., 11, 309-317, 1954.

Atlas, D., Matrosov, S. Y., Heymsfield, A. J., Chou, M.-D., and Wolff, D. B.: Radar and radiation properties of ice clouds, J. Appl. Meteorol., 34, 2329-2345, 1995.

Battaglia, A., and Delanoë, J.: Synergies and complementarities of CloudSat-CALIPSO snow observations, J. Geophys. Res.: Atmos., 118, 721-731, 2013.

Battan, L. J.: Radar observation of the atmosphere, University of Chicago, Chicago, Illinois, 1973.

809   Bodas-Salcedo, A., Webb, M., Bony, S., Chepfer, H., Dufresne, J.-L., Klein, S., Zhang, Y.,
810 Marchand, R., Haynes, J., and Pincus, R.: COSP: Satellite simulation software for model assessment, Bull.
811 Amer. Meteorol. Soc., 92, 1023-1043, 2011.

812   Bretherton, C. S., and Park, S.: A new moist turbulence parameterization in the Community
813 Atmosphere Model, J. Climate, 22, 3422-3448, 2009.

814   Cesana, G., and Chepfer, H.: Evaluation of the cloud thermodynamic phase in a climate model
815 using CALIPSO-GOCCP, J. Geophys. Res.: Atmos., 118, 7922-7937, 2013.

816   Chepfer, H., Bony, S., Winker, D., Chiriaco, M., Dufresne, J. L., and Sèze, G.: Use of CALIPSO
817 lidar observations to evaluate the cloudiness simulated by a climate model, Geophys. Res. Lett., 35, 2008.

818   de Boer, G., Eloranta, E. W., and Shupe, M. D.: Arctic mixed-phase stratiform cloud properties
819 from multiple years of surface-based measurements at two high-latitude locations, J. Atmos. Sci., 66, 2874-
820 2887, 2009.

821   Dong, X., and Mace, G. G.: Arctic stratus cloud properties and radiative forcing derived from
822 ground-based data collected at Barrow, Alaska, J. climate, 16, 445-461, 2003.

823   English, J. M., Kay, J. E., Gettelman, A., Liu, X., Wang, Y., Zhang, Y., and Chepfer, H.:
824 Contributions of clouds, surface albedos, and mixed-phase ice nucleation schemes to Arctic radiation biases
825 in CAM5, J. Climate, 27, 5174-5197, 2014.

826   Fox, N. I., and Illingworth, A. J.: The retrieval of stratocumulus cloud properties by ground-based
827 cloud radar, J. Appl. Meteorol., 36, 485-492, 1997.

828   Frey, W., Maroon, E., Pendergrass, A., and Kay, J.: Do Southern Ocean Cloud Feedbacks Matter
829 for 21st Century Warming?, Geophys. Res. Lett., 2017.

830   Gettelman, A., and Morrison, H.: Advanced two-moment bulk microphysics for global models. Part
831 I: Off-line tests and comparison with other schemes, J. Climate, 28, 1268-1287, 2015.

832   Gettelman, A., Morrison, H., Santos, S., Bogenschutz, P., and Caldwell, P.: Advanced two-moment
833 bulk microphysics for global models. Part II: Global model solutions and aerosol–cloud interactions, J.
834 Climate, 28, 1288-1307, 2015.

835   Hagen, M., and Yuter, S. E.: Relations between radar reflectivity, liquid-water content, and rainfall
836 rate during the MAP SOP, Quart. J. Roy. Meteorol. Soc.al Society, 129, 477-493, 2003.

837   Haynes, J., Luo, Z., Stephens, G., Marchand, R., and Bodas-Salcedo, A.: A multipurpose radar
838 simulation package: QuickBeam, Bull. Amer. Meteorol. Soc., 88, 1723-1727, 2007.

839   Heymsfield, A., Winker, D., Avery, M., Vaughan, M., Diskin, G., Deng, M., Mitev, V., and
840 Matthey, R.: Relationships between ice water content and volume extinction coefficient from in situ
841 observations for temperatures from 0 to– 86° C: Implications for spaceborne lidar retrievals, J. Appl.
842 Meteorol. Climatol., 53, 479-505, 2014.

843   Heymsfield, A. J., Winker, D., and van Zadelhoff, G. J.: Extinction-ice water content-effective
844 radius algorithms for CALIPSO, Geophys. Res. Lett., 32, 2005.

Geoscientific
Model Development
Discussions

845   Hogan, R. J., Illingworth, A., O'connor, E., and Baptista, J.: Characteristics of mixed-phase clouds.
846   II: A climatology from ground-based lidar, Quart. J. Roy. Meteorol. Soc.al Society, 129, 2117-2134, 2003.

847   Hogan, R. J., Behera, M. D., O'Connor, E. J., and Illingworth, A. J.: Estimate of the global
848   distribution of stratiform supercooled liquid water clouds using the LITE lidar, Geophys. Res. Lett., 31,
849   2004.

850   Hogan, R. J., and O'Connor, E.: Facilitating cloud radar and lidar algorithms: The Cloudnet
851   Instrument Synergy/Target Categorization product, Cloudnet documentation, 2004.

852   Hogan, R. J., Mittermaier, M. P., and Illingworth, A. J.: The retrieval of ice water content from
853   radar reflectivity factor and temperature and its use in evaluating a mesoscale model, J. Appl. Meteorol.
854   Climatol., 45, 301-317, 2006.

855   Hu, Y., Vaughan, M., Liu, Z., Lin, B., Yang, P., Flittner, D., Hunt, B., Kuehn, R., Huang, J., and
856   Wu, D.: The depolarization-attenuated backscatter relation: CALIPSO lidar measurements vs. theory,
857   Optics Express, 15, 5327-5332, 2007a.

858   Hu, Y., Vaughan, M., McClain, C., Behrenfeld, M., Maring, H., Anderson, D., Sun-Mack, S.,
859   Flittner, D., Huang, J., Wielicki, B., Minnis, P., Weimer, C., Trepte, C., and Kuehn, R.: Global statistics of
860   liquid water content and effective number concentration of water clouds over ocean derived from
861   combined CALIPSO and MODIS measurements, Atmos. Chem. Phys., 7, 3353--3359, 10.5194/acp-7-
862   3353-2007, 2007b.

863   Hu, Y., Winker, D., Vaughan, M., Lin, B., Omar, A., Trepte, C., Flittner, D., Yang, P., Nasiri, S. L.,
864   and Baum, B.: CALIPSO/CALIOP cloud phase discrimination algorithm, J. Atmos. Ocean. Technol., 26,
865   2293-2309, 2009.

866   Hu, Y., Rodier, S., Xu, K. m., Sun, W., Huang, J., Lin, B., Zhai, P., and Josset, D.: Occurrence,
867   liquid water content, and fraction of supercooled water clouds from combined CALIOP/IIR/MODIS
868   measurements, J. Geophys. Res.: Atmos., 115, 2010.

869   Huang, Y., Siems, S. T., Manton, M. J., Hande, L. B., and Haynes, J. M.: The structure of low-
870   altitude clouds over the Southern Ocean as seen by CloudSat, J. Climate, 25, 2535-2546, 2012a.

871   Huang, Y., Siems, S. T., Manton, M. J., Protat, A., and Delanoë, J.: A study on the low-altitude
872   clouds over the Southern Ocean using the DARDAR-MASK, J. Geophys. Res.: Atmos., 117, 2012b.

873   Intrieri, J., Shupe, M., Uttal, T., and McCarty, B.: An annual cycle of Arctic cloud characteristics
874   observed by radar and lidar at SHEBA, J. Geophys. Res.: Oceans, 107, 2002.

875   Kalesse, H., Szyrmer, W., Kneifel, S., Kollias, P., and Luke, E.: Fingerprints of a riming event on
876   cloud radar Doppler spectra: observations and modeling, Atmos. Chem. Phys., 16, 2997-3012, 2016.

877   Kay, J. E., Bourdages, L., Miller, N. B., Morrison, A., Yettella, V., Chepfer, H., and Eaton, B.:
878   Evaluating and improving cloud phase in the Community Atmosphere Model version 5 using spaceborne
879   lidar observations, J. Geophys. Res.: Atmos., 121, 4162-4176, 2016.

880   Kikuchi, K., Tsuboya, S., Sato, N., Asuma, Y., Takeda, T., and Fujiyoshi, Y.: Observation of
881   wintertime clouds and precipitation in the Arctic Canada (POLEX-North), J. Meteorol. Soc. Japan. Ser. II,
882   60, 1215-1226, 1982.

Geoscientific
Model Development
Discussions

883   Klein, S. A., McCoy, R. B., Morrison, H., Ackerman, A. S., Avramov, A., Boer, G. d., Chen, M.,
884   Cole, J. N., Del Genio, A. D., and Falk, M.: Intercomparison of model simulations of mixed-phase clouds
885   observed during the ARM Mixed-Phase Arctic Cloud Experiment. I: Single-layer cloud, Quart. J. Roy.
886   Meteorol. Soc., 135, 979-1002, 2009.

887   Kollias, P., Miller, M. A., Luke, E. P., Johnson, K. L., Clothiaux, E. E., Moran, K. P., Widener, K.
888   B., and Albrecht, B. A.: The Atmospheric Radiation Measurement Program cloud profiling radars: Second-
889   generation sampling strategies, processing, and cloud data products, J. Atmos. Ocean. Technol., 24, 1199-
890   1214, 2007.

891   Kollias, P., Rémillard, J., Luke, E., and Szyrmer, W.: Cloud radar Doppler spectra in drizzling
892   stratiform clouds: 1. Forward modeling and remote sensing applications, J. Geophys. Res.: Atmos., 116,
893   2011.

894   Kollias, P., Clothiaux, E. E., Ackerman, T. P., Albrecht, B. A., Widener, K. B., Moran, K. P., Luke,
895   E. P., Johnson, K. L., Bharadwaj, N., and Mead, J. B.: Development and applications of ARM millimeter-
896   wavelength cloud radars, Meteorological Monographs, 57, 17.11-17.19, 2016.

897   Kuehn, R., Holz, R., Eloranta, E., Vaughan, M., and Hair, J.: Developing a Climatology of Cirrus
898   Lidar Ratios Using Univeristy of Wisconsin HSRL Observations, EPJ Web of Conferences, 2016, 16009,

899   Liao, L., and Sassen, K.: Investigation of relationships between Ka-band radar reflectivity and ice
900   and liquid water contents, Atmospheric Res., 34, 231-248, 1994.

901   Liu, C.-L., and Illingworth, A. J.: Toward more accurate retrievals of ice water content from radar
902   measurements of clouds, J. Appl. Meteorol., 39, 1130-1146, 2000.

903   McCoy, D. T., Tan, I., Hartmann, D. L., Zelinka, M. D., and Storelvmo, T.: On the relationships
904   among cloud cover, mixed-phase partitioning, and planetary albedo in GCMs, J. Advances in Modeling
905   Earth Systems, 8, 650-668, 2016.

906   O'Connor, E. J., Illingworth, A. J., and Hogan, R. J.: A technique for autocalibration of cloud lidar,
907   J. Atmos. Ocean. Technol., 21, 777-786, 2004.

908   Rémillard, J., and Tselioudis, G.: Cloud regime variability over the Azores and its application to
909   climate model evaluation, J. Climate, 28, 9707-9720, 2015.

910   Sassen, K.: Ice cloud content from radar reflectivity, J. climate and Appl. Meteorol., 26, 1050-1053,
911   1987.

912   Sassen, K.: The polarization lidar technique for cloud research: A review and current assessment,
913   Bull. Amer. Meteorol. Soc., 72, 1848-1866, 1991.

914   Sato, N., Kikuchi, K., Barnard, S. C., and Hogan, A. W.: Some characteristic properties of ice
915   crystal precipitation in the summer season at South Pole Station, Antarctica, J. Meteorol. Soc. Japan. Ser.
916   II, 59, 772-780, 1981.

917   Sauvageot, H., and Omar, J.: Radar reflectivity of cumulus clouds, J. Atmos. Ocean. Technol., 4,
918   264-272, 1987.

Geoscientific
Model Development
Discussions

919   Schmidt, G. A., Kelley, M., Nazarenko, L., Ruedy, R., Russell, G. L., Aleinov, I., Bauer, M., Bauer,
920   S. E., Bhat, M. K., and Bleck, R.: Configuration and assessment of the GISS ModelE2 contributions to the
921   CMIP5 archive, J. Adv. Model. Earth Syst., 6, 141-184, 2014.

922   Sekhon, R. S., and Srivastava, R.: Doppler radar observations of drop-size distributions in a
923   thunderstorm, J. Atmos. Sci., 28, 983-994, 1971.

924   Shupe, M. D.: A ground-based multisensor cloud phase classifier, Geophys. Res. Lett., 34, 2007.

925   Tan, I., and Storelvmo, T.: Sensitivity study on the influence of cloud microphysical parameters on
926   mixed-phase cloud thermodynamic phase partitioning in CAM5, J. Atmos. Sci., 73, 709-728, 2016.

927   Tan, I., Storelvmo, T., and Zelinka, M. D.: Observational constraints on mixed-phase clouds imply
928   higher climate sensitivity, Science, 352, 224-227, 2016.

929   Tatarevic, A., and Kollias, P.: User's Guide to Cloud Resolving Model Radar Simulator (CR-SIM),
930   McGill University Clouds Research Group, Document available at http://radarscience.weebly.com/radar-
931   simulators.html. 2015.

932   Yoshida, R., Okamoto, H., Hagihara, Y., and Ishimoto, H.: Global analysis of cloud phase and ice
933   crystal orientation from Cloud-Aerosol Lidar and Infrared Pathfinder Satellite Observation (CALIPSO)
934   data using attenuated backscattering and depolarization ratio, J. Geophys. Res.: Atmos., 115, 2010.

935   Zhang, Y., Xie, S., Klein, S. A., Marchand, R., Kollias, P., Clothiaux, E. E., Lin, W., Johnson, K.,
936   Swales, D., and Bodas-Salcedo, A.: The ARM Cloud Radar Simulator for Global Climate Models: A New
937   Tool for Bridging Field Data and Climate Models, Bull. Amer. Meteorol. Soc., 2017.
938
939
940